experimentally are in accordance with such predictions.[4–6] It was shown in the measurements section that the plethora of structure in the electro-absorption spectrum at low electric fields was taken over by one broad positive peak as the field was raised above 5×10^4 V/cm. It was also shown that the final state in the transition process was an exciton state. We now wish to show that 5×10^4 V/cm is just the electric field strength which initiates field ionization of exciton states and thereby changes the energy distribution of these states. The binding energy of the exciton in Si has been determined to be 0.01 eV.[12,14] The radius of the first exciton Bohr orbit, a_0' in silicon is approximately $1\times6\times10^{-7}$ cm. The Stark effect for weakly bound excitons has been given as[20]

$$\Delta E=-\tfrac{3}{2}neEa_0', \tag{3}$$

for levels of principal quantum number n. Ionization of the level of principal quantum number 1 then onsets at an electric field strength of 5×10^4 V/cm. This is to be compared with the electric field strength range of 4×10^4–8×10^4 V/cm at which experimental results show a coalescence of structure into one broad positive electro-absorption peak.

PHYSICAL REVIEW VOLUME 140, NUMBER 4A 15 NOVEMBER 1965

Free-Carrier Magneto-Microwave Kerr Effect in Semiconductors*

M. E. Brodwin and R. J. Vernon†
Department of Electrical Engineering, Northwestern University, Evanston, Illinois
(Received 3 June 1965)

The free-carrier magneto-Kerr effect is analyzed in terms of R, the amplitude ratio of the two orthogonal linearly polarized components of the reflected wave, and δ, the phase difference between these two components. Equations relating R and δ to the elements of the magnetoconductivity tensor are presented for the plane-wave case and the TE_{11} mode in a circular waveguide. Simple approximate expressions for R and δ are given for the high-loss case where $\sigma_s/\omega\epsilon_s\gg1$, $\mu_H B\ll1$, and $\omega\tau\ll1$ (σ_s=zero-field dc conductivity; ϵ_s=static dielectric constant; μ_H=Hall mobility; τ=scattering time). These approximate expressions are compared with curves computed from the more complex expressions. The effect of multiple reflections within the semiconductor is considered. Experimental data for R and δ as functions of magnetic flux density and resistivity are presented for n-type germanium, n- and p-type silicon, and n-type indium antimonide at room temperature for the TE_{11} mode in a circular waveguide. It is found experimentally that the TE_{11}-mode analysis of the magneto-Kerr effect applies equally well to samples placed inside the circular waveguide and to those abutting on the end of the waveguide. Data on one n-type germanium and one n-type indium antimonide crystal are presented for temperatures between about 100 and 300°K. The effect of surface treatment on the measurements is also discussed.

I. INTRODUCTION

In recent years considerable attention has been given to the microwave Faraday effect in semiconductors.[1–6] It has been shown to be a powerful tool for the investigation of semiconductor transport parameters. However, since the Faraday effect depends upon transmission of electromagnetic radiation through the material, its measurement becomes difficult for the higher conductivity semiconductors where the energy transmitted through the sample is very small. In this high-conductivity range the magneto-Kerr effect, which occurs in the reflected wave, can often be measured. Because of its close relation to the Faraday effect, the magneto-Kerr effect can also be expected to yield valuable information concerning the semiconductor transport parameters.

The Kerr effect arises when a linearly polarized electromagnetic wave is incident upon the surface of a sample in the static magnetic field. The reflected wave is elliptically polarized with the major axis of the ellipse rotated with respect to the incident plane of polarization. Only the case of normal incidence with the magnetic field collinear with the direction of propagation is considered here. For this case, the origin of the ellipse can be explained qualitatively by considering the incident linearly polarized wave as being composed of two counter-rotating circularly polarized components. Since the lateral motions of the free-charge carriers in the static magnetic field are circular and in the same sense for all carriers of a given type, the two circularly polarized components react differently with the free-charge carriers. Thus, the two components have different reflection coefficients at the surface of the sample and,

* This work was supported by a National Defense Education Act Fellowship and the Advanced Research Projects Agency through the Northwestern University Materials Research Center.
† Present address: Electrical Engineering Department, University of Wisconsin, Madison, Wisconsin.
[1] R. Suhl and G. L. Pearson, Phys. Rev. **92**, 858 (1953).
[2] R. R. Rau and M. E. Caspari, Phys. Rev. **100**, 632 (1955).
[3] J. K. Furdyna and S. Broersma, Phys. Rev. **120**, 1995 (1960).
[4] J. K. Furdyna and M. E. Brodwin, Phys. Rev. **124**, 740 (1961).
[5] A. Bouwknegt and J. Volger, Physica **30**, 113 (1964).
[6] M. E. Brodwin and T. J. Burgess, Appl. Phys. Letters **5**, 223 (1964).

consequently, the total reflected wave is elliptically polarized.

The magneto-Kerr effect in semiconductors has received comparatively little attention in the literature. It was discussed by Lax and Zwerdling[7] in 1960 and observed by Brodwin, Furdyna, and Vernon[8] in 1961 at microwave frequencies in germanium. Palik *et al.*[9,10] reported on their observation of the magneto-Kerr effect in indium antimonide at infrared frequencies in 1962. Further discussion on a method of measuring the Kerr effect at microwave frequencies was given by Brodwin and Vernon[11] in 1963. The data presented below were obtained by the method discussed in that paper.

In this article the magneto-Kerr effect is analyzed in terms of R, the amplitude ratio of the two orthogonal linearly polarized components of the reflected wave, and δ, the phase difference between these two components. The analysis is carried out in terms of R and δ rather than rotation and ellipticity, because R and δ are the parameters measured directly by the experimental system. Expressions for rotation and ellipticity in terms of R and δ are given in Appendix B.

Equations relating R and δ to the elements of the magnetoconductivity tensor are presented for the plane-wave case, and for the TE_{11} mode in a circular waveguide. For the case of the TE_{11} mode, the treatment is restricted to the $\mu_H B \ll 1$ range, where μ_H is the Hall mobility. The effect of multiple reflections is discussed in Appendix C. Simple approximate expressions for R and δ are discussed for the high-loss, low-magnetic-field, low-$\omega\tau$ case. Finally, experimental results for n-type germanium, n-type and p-type silicon, and n-type indium antimonide are presented.

II. THEORY

A. The Conductivity Tensor

Consider a semiconductor in a uniform static magnetic field which is directed along the positive z axis. If this axis is parallel to the [100] or the [111] crystallographic direction for n-type germanium or n-type silicon, the magnetoconductivity tensor σ may be written in the form[12]

$$\sigma=\begin{bmatrix}\sigma_{11} & \sigma_{12} & 0\\ -\sigma_{12} & \sigma_{11} & 0\\ 0 & 0 & \sigma_{33}\end{bmatrix}. \tag{1}$$

In cases where the constant-energy surfaces for the majority carriers may be assumed to be spherical, e.g., n-type indium antimonide, this magnetoconductivity tensor is valid for any crystallographic orientation of the magnetic field. This discussion will be restricted to the case where the magnetic field is oriented along the [100] crystallographic direction in n-type germanium, the [111] direction in n-type silicon, or any direction in materials where spherical constant-energy surfaces may be assumed. For these cases, the elements of conductivity tensor are given in Appendix A for a high-frequency electric field. It is to be noted, however, that in the development which follows, expressions written explicity in terms of the elements of the conductivity tensor, and not depending on the equations of Appendix A, are valid whenever the tensor of Eq. (1) is valid.

B. The Plane-Wave Case

Now assume that the semiconductor has a flat surface in the xy plane and that incident upon this surface is a linearly polarized plane wave with its electric field in the x direction. If this linearly polarized wave is resolved into two counter-rotating circularly polarized components (+ and −), these two components have different propagation constants in the semiconductor, given by[12]

$$k_{\pm}^2=\omega^2\mu_0\epsilon_s-i\omega\mu_0(\sigma_{11}\mp i\sigma_{12}). \tag{2}$$

Here ω is the angular frequency of the incident wave, μ_0 the permeability of free space, and ϵ_s the static dielectric constant of the semiconductor. The convention has been used that the + subscript refers to a wave rotating from the positive x direction to the positive y direction independent of the direction of propagation. The − subscript refers to the opposite sense of rotation. The two circularly polarized waves also have different electric-field reflection coefficients at the semiconductor surface, given by

$$\rho_{\pm}=\frac{E_{r_{\pm}}(y=0)}{E_{i_{\pm}}(y=0)}=\frac{k_0-k_{\pm}}{k_0+k_{\pm}}, \tag{3}$$

where E_{i_+} and E_{i_-} represent the electric fields of the incident-wave components, E_{r_+} and E_{r_-} those of the reflected components, and k_0 is the free-space propagation constant.

Because these reflection coefficients are, in general, different in both magnitude and phase, the *total* reflected wave has a component E_{r_y} which is orthogonal to the linearly polarized mode of the incident wave. Let R be the magnitude of the ratio of the two orthogonal components of the reflected wave and δ the phase difference between them. Then it may be shown that

$$R\triangleq\left|\frac{E_{r_y}}{E_{r_x}}\right|=\left|\frac{\rho_+-\rho_-}{\rho_++\rho_-}\right|=k_0\left|\frac{k_+-k_-}{k_0^2-k_+k_-}\right|, \tag{4}$$

---

[7] B. Lax and S. Zwerdling, in *Progress in Semiconductors*, edited by A. F. Gibson (Academic Press Inc., New York, 1960), Vol. 5, p. 260.

[8] M. E. Brodwin, J. K. Furdyna, and R. J. Vernon, Bull. Am. Phys. Soc. **6**, 427 (1961).

[9] E. D. Palik, B. W. Henvis, and S. Teitler, Bull. Am. Phys. Soc. **7**, 184 (1962).

[10] E. D. Palik, S. Teitler, B. W. Henvis, and R. F. Wallis, in *Proceedings of the Conference on Semiconductor Physics* (Academic Press Inc., New York, 1962), Vol. 6, p. 288.

[11] M. E. Brodwin and R. J. Vernon, Rev. Sci. Instr. **34**, 1129 (1963).

[12] B. Lax and L. M. Roth, Phys. Rev. **98**, 548 (1955).

and

$$\delta \triangleq \arg\left(\frac{E_{ry}}{E_{rx}}\right) = -\frac{\pi}{2} + \arg\left[\frac{\rho_+ - \rho_-}{\rho_+ + \rho_-}\right] = \frac{\pi}{2} + \arg\left[\frac{k_+ - k_-}{k_0^2 - k_+ k_-}\right]. \quad (5)$$

It has been assumed that the semiconductor crystal is sufficiently thick so that multiple reflections within the sample can be neglected in the analysis of the magneto-Kerr effect. For the high-conductivity semiconductors and low magnetic fields, sufficient thicknesses greater than about five skin-depths will adequately eliminate multiple reflections. In the case of the Faraday effect, a careful balance between loss of transmitted power and the effect of multiple reflections must be achieved if a simple single-transmission analysis is to be used.

If the semiconductor sample is less than about five skin-depths thick it is necessary to consider the effect of multiple reflections within the crystal. The effects of multiple reflections on R and δ are considered in Appendix C.

C. The TE_{11} Mode in a Circular Waveguide

The case of propagation of the TE_{11} mode in a semiconductor-filled circular waveguide in a longitudinal static magnetic field has been considered by several authors.[13–16] The discussion given here uses the results of the treatment by Champlin[16] which employs perturbation methods for low magnetic fields ($\mu_H B \ll 1$). For this case the propagation constants for the two counter-rotating circularly polarized TE_{11} waves in the semiconductor are given by

$$k_{g\pm}^2 = \omega^2 \mu_0 \epsilon_s - i\omega\mu_0(\sigma_{11} \mp iK\sigma_{12}) - k_c^2, \quad (6)$$

where $K=0.838$, $k_c = 1.841/a$ for the TE_{11} mode, and a is the radius of the waveguide. Then, for the case of the guided wave

$$R_g = k_{g0}\left|\frac{k_{g+} - k_{g-}}{k_{g0}^2 - k_{g+}k_{g-}}\right| \quad (7)$$

and

$$\delta_g = \frac{\pi}{2} + \arg\left[\frac{k_{g+} - k_{g-}}{k_{g0}^2 - k_{g+}k_{g-}}\right], \quad (8)$$

where k_{g0} is the propagation constant in the empty waveguide, given by

$$k_{g0} = [k_0^2 - k_c^2]^{1/2}. \quad (9)$$

The values of R_g and δ_g predicted by these equations will be compared with experimental results in Sec. III.

[13] H. Suhl and L. R. Walker, Phys. Rev. **96**, 121, (1952).
[14] H. Suhl and L. R. Walker, Bell System Tech. J. **33**, 1122 (1954).
[15] H. Gamo, J. Phys. Soc. Japan **8**, 176 (1953).
[16] K. S. Champlin, Physica **28**, 1143 (1962).

D. Approximate Expressions for the High-Loss Case

The high-loss case is of special interest when considering the magneto-Kerr effect. The high-loss case occurs when $\sigma_s/\omega\epsilon_s \gg 1$, $\omega_c\tau \ll 1$, and $\omega\tau \ll 1$; where σ_s is the dc conductivity for zero magnetic field, ω_c is the cyclotron angular frequency, and τ is the scattering time. For this case we have the following relations in terms of the elements of the conductivity tensor: $\sigma_{11}'/\omega\epsilon_s \gg 1$, $\sigma_{11}' \gg |\sigma_{11}''|$, and $\sigma_{11}' \gg |\sigma_{12}'| \gg |\sigma_{12}''|$. Here the single prime denotes the real part of the element, and the double prime, the imaginary part. It is also assumed that the relative static dielectric constant κ_s is much greater than unity. When these conditions hold, the following approximate relations may be obtained from the previous equations for the plane-wave case:

$$R \approx \frac{|\sigma_{12}'|}{\sigma_{11}'}\left(\frac{\omega\epsilon_0}{\sigma_{11}'}\right)^{1/2} \approx \frac{m_\sigma}{m_c}\frac{\omega_c\langle\tau^2\rangle}{\langle\tau\rangle}\left(\frac{\omega\epsilon_0}{\sigma_s}\right)^{1/2} = \mu_H B\left(\frac{\omega\epsilon_0}{\sigma_s}\right)^{1/2}, \quad (10)$$

$$\delta \approx (5/4)\pi + (\sigma_{12}''/\sigma_{12}') - (1/\sigma_{11}')[\tfrac{3}{2}\sigma_{11}'' + \omega\epsilon_0(\tfrac{3}{2}\kappa_s - 1)] \text{ radians}, \quad qB>0, \quad (11)$$

$$\delta \approx \frac{5\pi}{4} - \frac{\omega\epsilon_s}{\sigma_s}\left(\frac{3}{2} - \frac{1}{\kappa_s}\right) - \omega\langle\tau\rangle\left[2\frac{\langle\tau^3\rangle}{\langle\tau^2\rangle\langle\tau\rangle} - \frac{3}{2}\frac{\langle\tau^2\rangle}{\langle\tau\rangle^2}\right] \text{ radians}, \quad qB>0, \quad (12)$$

where ϵ_0 is the permittivity of free space and μ_H is the Hall mobility. For a general function of energy $g(\mathcal{E})$, the symbol $\langle g(\mathcal{E})\rangle$ represents the integral

$$\langle g(\mathcal{E})\rangle = \frac{4}{3\pi^{1/2}(kT)^{5/2}}\int_0^\infty g(\mathcal{E})\mathcal{E}^{3/2}e^{-\mathcal{E}/kT}\,d\mathcal{E} \quad (13)$$

for the case of nondegenerate semiconductors. For the case of strong degeneracy $\langle g(\mathcal{E})\rangle \approx g(\mathcal{E}_F)$ where $\mathcal{E}_F$ is the Fermi energy. For intermediate cases exact Fermi-Dirac statistics must be used.[17] If we assume τ is energy independent, Eq. (12) reduces to

$$\delta \approx (\tfrac{5}{4})\pi - (\omega\epsilon_s/\sigma_s)[(\tfrac{3}{2} - (1/\kappa_s)] - \tfrac{1}{2}\omega\tau \text{ radians}, \quad qB>0. \quad (14)$$

Equations (11), (12), and (14) are written for the case of $qB>0$ where q is the charge of the majority carriers; positive for holes and negative for electrons. B is taken as positive when it is directed along the positive z axis and negative when it is directed along the negative z axis. If the sign of either q or B reverses, δ changes by 180°. This may be explained by noting that in obtaining Eq. (11) from Eq. (5) there arises an equa-

[17] A. C. Beer, *Galvanomagnetic Effects in Semiconductors* (Academic Press Inc., New York, 1963), p. 107.

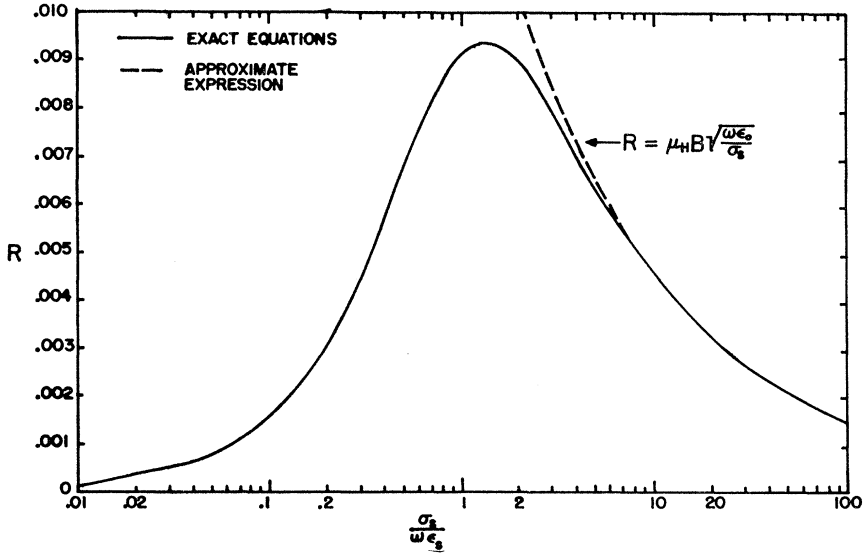

FIG. 1. Graph of computed values of R versus $\sigma_s/\omega\epsilon_s$ for silicon, assuming energy-independent scattering and spherical constant-energy surface; $\kappa_s=11.7$, $\mu_H B=0.05$, $\omega\tau=0.01$.

tion of the form

$$\delta=\frac{\pi}{2}+\tan^{-1}\left\{\frac{(qB)[1-f_1(\sigma_{11},\sigma_{12})]}{(-qB)[1-f_2(\sigma_{11},\sigma_{12})]}\right\}, \qquad (15)$$

where $|f_1|\ll 1$, $|f_2|\ll 1$ and only even powers of qB appear in f_1 and f_2. Thus a change in sign of qB changes δ by 180°.

In order to check the accuracy of these approximations in their range of validity, they are plotted along with curves obtained from the exact equations, Eqs. (2) through (5) and (A1) through (A4), assuming an energy-independent scattering, spherical constant-energy-surface model. Note that for this model there is no distinction between Hall and conductivity mobility, but the symbol μ_H will still be used for continuity with the preceding development. Figure 1 shows the exact and approximate curves for R versus $\sigma_s/\omega\epsilon_s$ for silicon with $\kappa_s=11.7$, $\mu_H B=0.05$, and $\omega\tau=0.01$. The parameter which is being varied here is actually σ_s. However, R is plotted against $\sigma_s/\omega\epsilon_s$ since this is the parameter which determines when the approximate expression is in its range of validity ($\sigma_s/\omega\epsilon_s\gg 1$). Note that the approximate expression fits the exact curve quite closely for $\sigma_s/\omega\epsilon_s$ greater than about 5. Figure 1 shows that R is a maximum near $\sigma_s/\omega\epsilon_s=1$ which may be checked by differentiating the exact equations and using $\mu_H B$, $\omega\tau\ll 1$.

Figure 2 shows the exact and approximate curves for δ versus $\sigma_s/\omega\epsilon_s$ for silicon with $\kappa_s=11.7$, $\mu_H B=0.05$, and $\omega\tau=0.01$. Here again σ_s is the parameter which is actually being varied. The approximate expression agrees very well with the exact curve for $\sigma_s/\omega\epsilon_s$ greater than about 2.

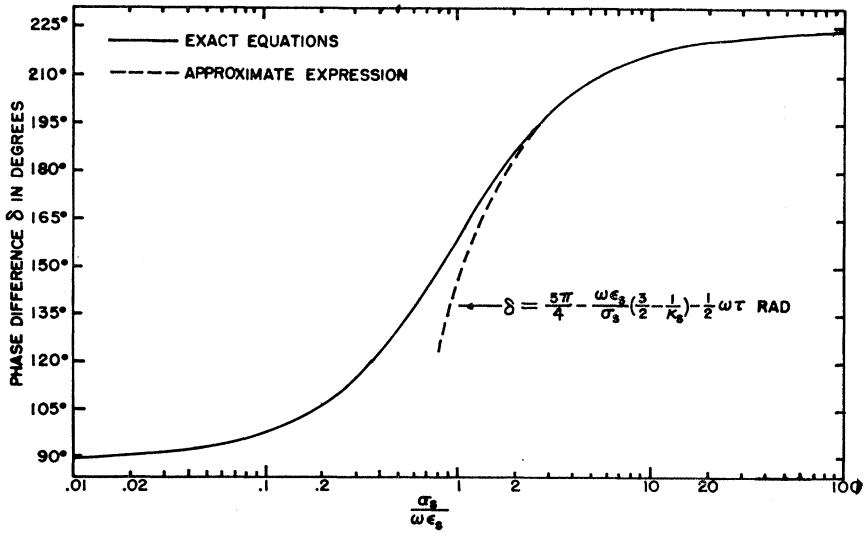

FIG. 2. Graph of computed values of δ versus $\sigma_s/\omega\epsilon_s$ for silicon assuming energy-independent scattering and spherical constant-energy surfaces; $\kappa_s=11.7$, $\mu_H B=0.05$, $\omega\tau=0.01$.

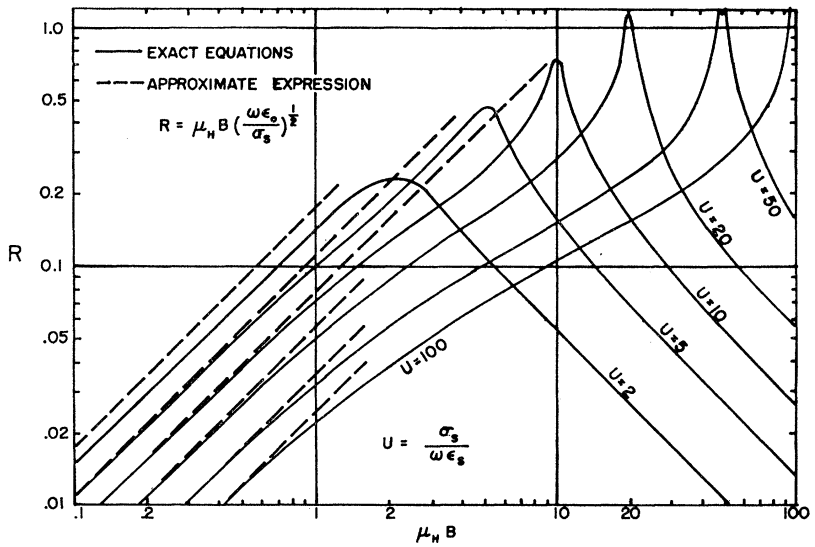

FIG. 3. Graph of R as a function of $\mu_H B$ for germanium assuming energy-independent scattering and spherical energy surfaces; $\kappa_s=16.27$, $\omega\tau=0.01$.

Figure 3 shows curves of R versus $\mu_H B$ for the exact equations and the high-loss approximation for several values of $\sigma_s/\omega\epsilon_s$ between 2 and 100. These curves are for germanium, $\kappa_s=16.27$. In the region where $\mu_H B \ll 1$ and $\sigma_s/\omega\epsilon_s \gg 1$ the approximate expressions fit the exact curve quite closely. However, for $\sigma_s/\omega\epsilon_s=2$ the approximate curve does not agree very well with the exact curve even for low $\mu_H B$, as could be predicted from Fig. 1. Although the exact curves in this figure are continued into the range where $\mu_H B \gg 1$, their accuracy in this region may be relatively poor compared with an energy-dependent τ treatment. However, qualitative agreement can be expected on the basis of the high-magnetic-field calculations of Brodwin and Burgess[6] for the case of lattice scattering. Note that for the simple model being considered here, R reaches a maximum at $\mu_H B \approx \sigma_s/\omega\epsilon_s$ for the case of $\sigma_s/\omega\epsilon_s \gg 1$. This is the point where ϵ_+' is zero, passing from a negative region to a positive region, while ϵ_-' is approximately equal to $2\epsilon_s$. Also, $\epsilon_+'' \approx \epsilon_-'' \approx \omega\epsilon_s^2/\sigma_s$ which is small compared to ϵ_-'. Thus there is a large difference between the propagation constants of the two counter-rotating circular polarizations under these conditions and consequently a large difference between the two reflection coefficients. For values of $\mu_H B \gg \sigma_s/\omega\epsilon_s \gg 1$, the $\mu_H B$ dependence of R is given by $R \propto 1/\mu_H B$.

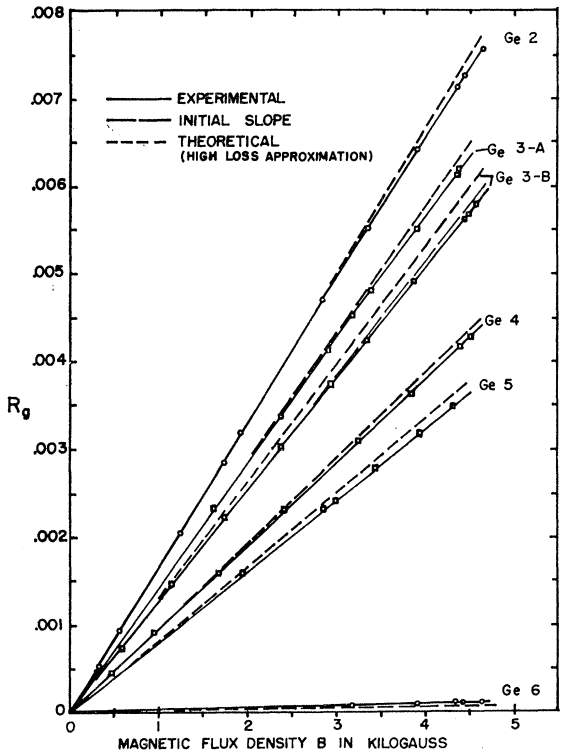

FIG. 4. Graph of R_g versus magnetic flux density for germanium samples at room temperature (300°K).

Approximate expressions for the high-loss range may also be derived for the case where the sample is enclosed in a circular waveguide and the incident wave is the TE_{11} mode. These approximations may be expressed in terms of those already derived for the plane-wave case. Thus, for the TE_{11} mode in a circular waveguide

$$R_g \approx K[1-(k_c^2/k_0^2)]^{1/2} R, \tag{16}$$

$$\delta_g \approx \delta. \tag{17}$$

Note that δ_g for the guided wave case is, for practical purposes, identical to δ for the plane wave, for the high-loss range, and R_g differs from R only by a multiplicative factor dependent solely on the frequency and the radius of the circular waveguide.

III. EXPERIMENTAL METHODS AND RESULTS

The magneto-microwave Kerr effect has been measured for the case of the TE_{11} mode in a 1-in.-diam

TABLE I. Information on samples (all n type).

Sample number	Mounting	Average resistivity room-temperature at $r \approx \frac{1}{4}$ in. (Ω-cm)
Ge 2	inside	1.45
Ge 3A	outside	1.12
Si n-3	outside	1.07
InSb	outside	0.00393

circular waveguide at a frequency of 8.98 Gc/sec. Measurements have been made on several n-type germanium and n- and p-type silicon samples, and one indium antimonide sample. The experimental system which was used to measure the magneto-microwave Kerr effect in semiconductors was a form of microwave interferometer employing a four-arm turnstile waveguide junction. The system has been described in detail in a previous article.[11] It allows R_g and δ_g to be measured simultaneously.

In the theoretical analysis of the magneto-Kerr effect for the Te_{11} mode in a circular waveguide, it was assumed that the semiconductor was inserted *into* the waveguide completely filling the cross section. In practice two different methods of mounting the sample were used. In the first method the sample was inserted *into* the waveguide. Other larger samples were simply affixed to the end of the tube with conductive silver "paint" or adhesive cement. No difference in experimental results was observed between the two methods of affixing the sample to the outside of the tube, but the conductive silver paint helped eliminate radiation from the tube-sample joint. It was also found that there was no significant difference in results between locating the samples inside the tube and affixing them to the end of the tube, at least up to resistivities of about 3 Ω cm. That is, for both methods of mounting the sample, the results were in good agreement with the theoretical predictions for the TE_{11} mode.

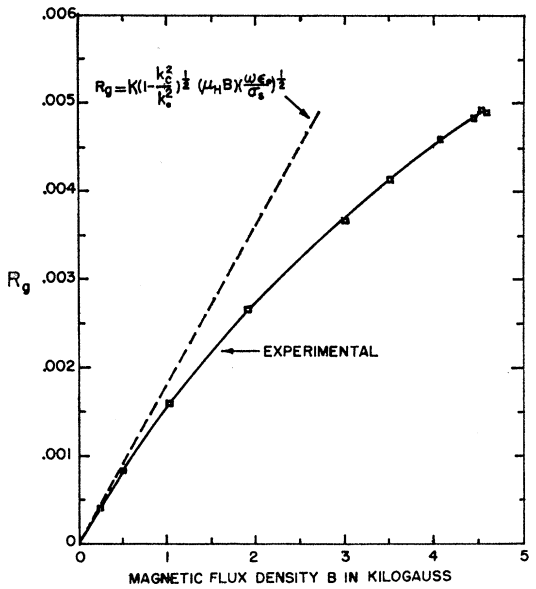

FIG. 5. Graph of R_g versus magnetic flux density for InSb at room temperature (300°K).

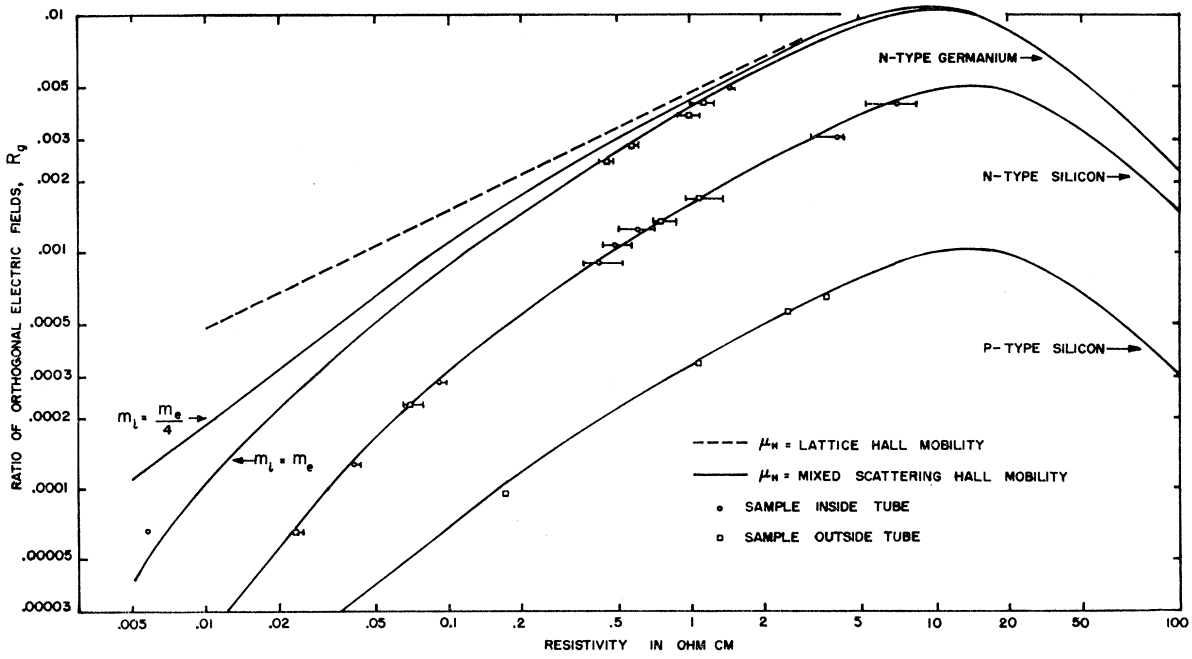

FIG. 6. Graph of R_g versus resistivity for $B=3$ kG, room temperature.

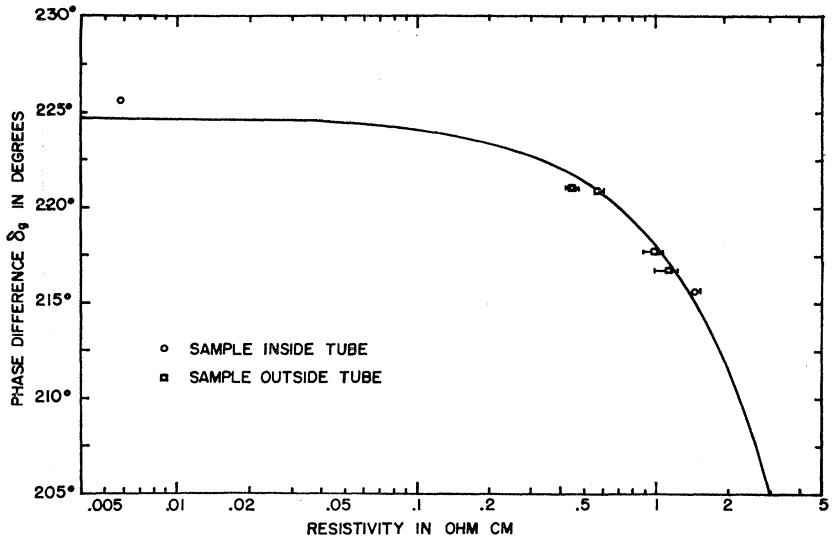

FIG. 7. Graph of δ_g versus resistivity for n-type germanium at room temperature.

The samples to be discussed here were all more than 8 skin-depths thick. All the germanium samples were n-type, and all were mounted so that the magnetic field was applied in the [100] crystallographic direction. All silicon samples, n type and p type, were mounted so that the magnetic field was applied along the [101] crystallographic direction. The n-type indium antimonide sample was polycrystalline, which should not affect the room-temperature results too greatly since the constant-energy surfaces are spherical near the minimum of the conduction band. Table I gives pertinent information for several of the samples to be considered for special purposes.

A. Room-Temperature Measurements

The values of R_g and δ_g have been measured at room temperature for these samples as a function of magnetic flux density B from 0 to about 5 kG. It was found that R_g varied linearly with B in the range $\mu_H B \ll 1$ for all samples, as is predicted by the theory. Figure 4 shows the variation of R_g with B for the germanium samples along with the theoretical predictions (the lines of short dashes) based on the approximation for the TE_{11} mode given by Eq. (16). The calculated curves for R_g used the measured value of conductivity at $r \approx \frac{1}{4}$ in. from the center of the sample,[18] and values of Hall mobility obtained from Debye and Conwell.[19] Note that the experimental curves for the higher purity samples (those with the lower numbers) begin to depart from linearity by a slight amount at the higher magnetic fields. This is due to the fact that the higher purity samples have greater Hall mobilities and thus leave the $\mu_H B \ll 1$ range at lower magnetic fields. A line of long dashes is used to indicate the initial slope of one of the experimental curves so that this departure from linearity can be seen more easily. This nonlinear behavior is of course more pronounced in Fig. 5 of R_g versus B for InSb which has a much higher Hall mobility ($\mu_H = 77\,000$ cm^2/V-sec in fairly pure n-type InSb at room temperature whereas $\mu_H \approx 4000$ cm^2/V-sec for sample Ge 1 at room temperature). R_g was found to be the same for positive- and negative-directed B. The graphs of R_g versus B are not shown for n- or p-type silicon since they were all linear and can be deduced from Fig. 6 which is discussed next.

Figure 6 shows graphs of R_g versus resistivity for n-type germanium and n-type and p-type silicon, at room temperature and a magnetic flux density of 3 kG. Here the horizontal lines drawn through the experimental points represent the variation in resistivity over the surface of the sample. The circle or square is drawn around the point of average resistivity at a distance of $\frac{1}{4}$ in. from the center of the sample. A circle indicates the sample was mounted inside the circular tube and a square indicates the sample was mounted outside.

The curves in Fig. 6 are theoretical predictions using Eqs. (6) through (9) for the TE_{11} mode and Eqs. A1 through A4 for the case of energy-independent scattering. The static dielectric constants used were 16.27 for germanium and 11.7 for silicon. The values of longitudinal and transverse effective masses used were $m_L = 1.64\ m_e$, $m_T = 0.0819\ m_e$ for n-type germanium, and $m_L = 0.98\ m_e$, $m_T = 0.19$ for n-type silicon. A single spherical-energy-surface model was used for p-type silicon. The dashed line for germanium was obtained by assuming that lattice scattering mobility (taken to be 4250 cm^2/V sec [19]) could be used throughout the resistivity range. The remaining curves assume mixed scattering in calculating theoretical Hall mobility. The mixed-scattering R_g-versus-resistivity curves for germanium were obtained using theoretical Hall mobilities taken from Debye and Conwell[19] which were calculated

[18] There was considerable variation of conductivity over the faces of several of the samples, as will be discussed further on in the paper.

[19] P. P. Debye and E. M. Conwell, Phys. Rev. 93, 693 (1954).

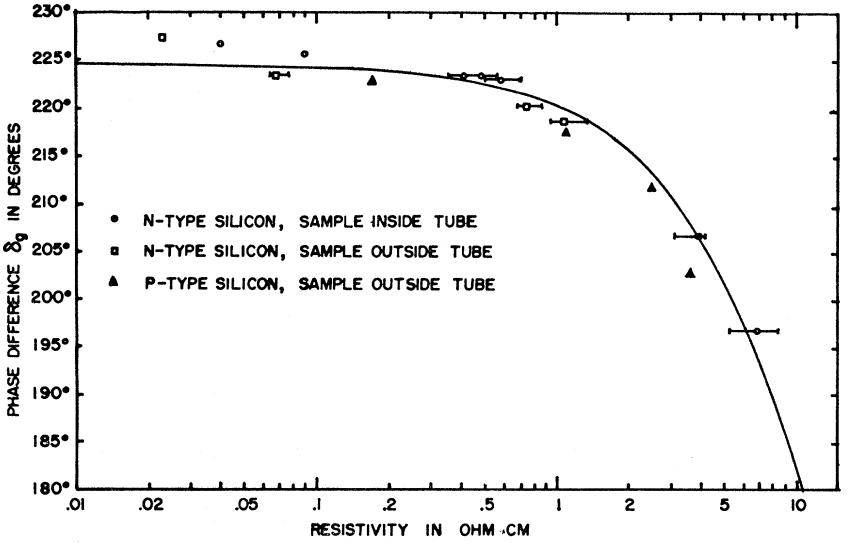

FIG. 8. Graph of δ_g versus resistivity for silicon at room temperature.

using the Brooks-Herring ionized-impurity scattering formula. One of these curves uses a value of $m_i=\frac{1}{4}m_e$ in this formula; the second uses $m_i=m_e$. Here m_e is the electronic mass and m_i is the ionized impurity scattering effective mass. Note that the experimental data agree best with the theoretical curve for $m_i=m_e$. The R-versus-resistivity curves for n- and p-type silicon were obtained using the theoretical mixed-scattering Hall mobility given by Morin and Maita.[20] It can be seen that there is no significant difference, in relation to the theoretical curves, between samples mounted inside the circular waveguide and those mounted outside.

The phase difference δ_g was found to remain constant (to within 1°) as the magnetic field was varied throughout the low magnetic field range. This is as predicted by Eq. (14). However, δ_g changed by 180° when the magnetic field was reversed. It was also found that p-type silicon samples produced values of δ_g differing by about 180° from n-type silicon samples of roughly the same resistivity. These observations also agree with theoretical predictions.

Figures 7 and 8 show the experimental values of δ_g plotted against resistivity, along with the theoretical curves again obtained from Eqs. (6) through (9) using an energy-independent τ model. The values of δ_g were measured for negative magnetic fields for n-type samples, and positive magnetic fields for p-type samples so that $qB>0$ for both cases. In this way the experimental points for n- and p-type silicon can be plotted on the same graph. The lines drawn through the experimental points again represent the variation of the resistivity over the face of the sample. Note that the points are much more scattered for the silicon samples. This is believed to be due primarily to the fact that since R_g is smaller in the silicon samples, the interferometer unbalance signals are therefore smaller, thus reducing the accuracy. The error in δ_g (including interferometer phase-calibration uncertainty[11]) is estimated to be less than $\pm 2°$ for nearly all samples. Furthermore, it can be seen in Figs. 7 and 8 that there is no significant difference, in relation to the theoretical curves, between samples mounted inside the circular waveguide and those mounted outside.

B. The Effect of Surface Treatment on R_g and δ_g

The theoretical expressions for the magneto-Kerr effect are obtained by matching boundary conditions at the air-semiconductor interface. It is assumed in this derivation that the surface of the semiconductor is completely smooth and has the identical properties as the bulk semiconductor right up to the interface. This situation cannot, of course, be produced even for surfaces cleaved in a high vacuum, since Tamm surface states would still exist even under these conditions. It is not immediately clear, then, how conditions, such as surface roughness, oxide layer, and surface charge layer, will affect the parameters measured. The effect of several different surface treatments on measured values of R_g and δ_g will be discussed below.

It was found experimentally that there was no observable differences in R_g or δ_g when the crystal surfaces were polished with grits from 1 to 30 μ. Also, no change in results was observed when samples were placed in air at room temperature for several days after polishing, allowing the oxide layer to increase. This is to be expected since the thicknesses of the oxide layer increase relatively slowly after the first hour.[21]

The parameters R_g and δ_g were measured on germanium sample 3A for ambient atmospheres of oxygen, dry nitrogen, nitrogen with methyl alcohol vapor, and

[20] F. J. Morin and J. P. Maita, Phys. Rev. 96, 28 (1954).

[21] S. P. Wolsky, J. Phys. Chem. Solids 8, 114 (1959).

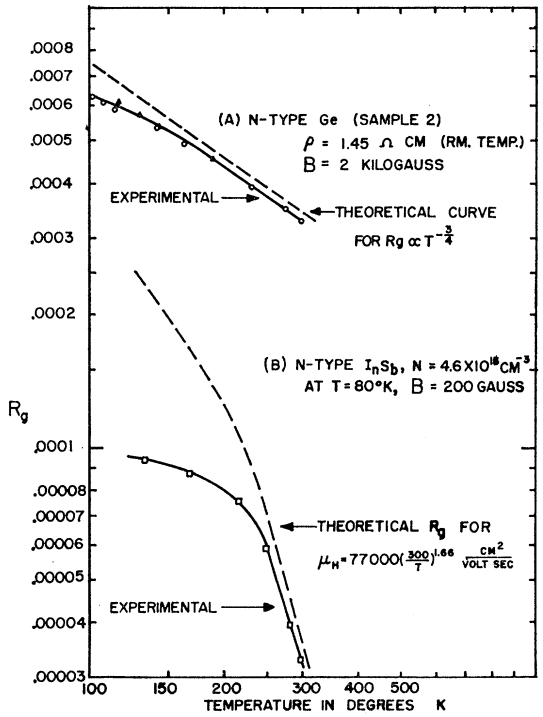

FIG. 9. Graph of R_g versus temperature for (a) germanium sample 2 and (b) the InSb sample.

wet air. Such variations of ambient atmosphere can be expected to change the semiconductor's surface properties, such as conductance and barrier height.[22] However, no change was observed in R_g or δ_g.

Finally, a layer of germanium from a 1.9-Ω-cm, n-type crystal was evaporated onto the surface of silicon sample n-3 (n-type, about 1.1 Ω-cm). The layer was about 3×10^{-5} cm thick. This is the order of magnitude of the extension of the space-charge region into the semiconductor. Again, no significant difference in R_g or δ_g was observed between readings taken before and after the evaporation.

It appears then, that provided the incident surface is flat and sufficiently smooth, surface conditions are not normally of significant importance. This is in agreement with some recent work done at optical frequencies with metals, by Stern, McGroddy, and Harte.[23]

C. Variation of R_g and δ_g with Temperature

Values of R_g and δ_g have also been measured as a function of temperature for an n-type germanium sample (Ge2) and an n-type indium antimonide sample. The samples were cooled by passing cold nitrogen gas through a chamber surrounding the sample and the end of the circular waveguide. Figure 9(a) shows the experimental curve for R_g versus T for the germanium sample at $B=2$ kG, along with the theoretically predicted curve assuming pure lattice scattering and constant carrier concentration. Since the dopant in this crystal is arsenic, it is safe to assume that the carrier concentration is relatively constant over the temperature range considered. Then, for the case of pure lattice scattering, where theory predicts $\langle\tau\rangle_L\alpha T^{-3/2}$, it is expected from Eq. (10) that $R_g\alpha T^{-3/4}$. This is the case in the higher temperature range. The deviation from this variation at lower temperatures is believed to be due to the increasing importance of ionized-impurity scattering at low temperatures.

Figure 9(b) shows experimental and theoretically predicted curves of R_g versus temperature for the InSb sample at $B=200$ G. It is necessary to confine the discussion to such a low field for InSb in order to remain in the range $\mu_H B\ll1$. In Fig. 9(b) the theoretical curve is based on measured values of conductivity and an assumed variation of Hall mobility given by[24]

$$\mu_H=77\,000(300/T)^{1.66}\ \text{cm}^2/\text{V/sec}, \qquad (18)$$

which assumes pure lattice scattering. Here the large departure from the theoretical slope at lower temperatures is again believed to be due primarily to ionized-impurity scattering. However, since the InSb sample is polycrystalline, it is also probable that scattering from crystal-grain boundaries also becomes significant at the lower temperatures.

Figure 10 shows the experimental and theoretically predicted variation of δ_g with temperature for the germanium sample (Ge2). The solid line is the experimental curve. The curve of long dashes gives the theoretical values predicted by Eq. (12) using measured values of conductivity, assuming an energy dependence for τ of $E^{-1/2}$ as for lattice scattering, and taking[25]

$$\langle\tau\rangle=2.39\times10^{-13}(300/T)^{1.53}\ \text{sec}. \qquad (19)$$

Here $T^{-1.53}$ was the measured temperature dependence of the conductivity, which is used since the carrier concentration may be assumed to be constant over the temperature range being considered. Note that agreement between this theoretical curve and the experimental curve is rather poor and believed to be out of the range of the experimental error.

The curves of short dashes are also calculated from Eq. (12) but with the $\omega\langle\tau\rangle[2\langle\tau^3\rangle/\langle\tau^2\rangle\langle\tau\rangle-\frac{3}{2}\langle\tau^2\rangle/\langle\tau\rangle^2]$ term deleted. Here $\sigma_s\alpha T^{-1.66}$ was the temperature dependence for pure lattice scattering in n-type germanium measured by Morin and Maita.[20] These curves, which neglect the $\omega\langle\tau\rangle$ term, lie much closer to the experimental curves.

[22] W. H. Brattain and J. Bardeen, Bell System Tech. J. **32**, 1 (1953).
[23] E. A. Stern, J. C. McGroddy, and W. E. Harte, Phys. Rev. **135**, A1306 (1964).
[24] O. Madelung, *Physics of* III-V *Compounds* (John Wiley & Sons, Inc., New York, 1964), p. 115.
[25] M. B. Prince, Phys. Rev. **82**, 681 (1953).

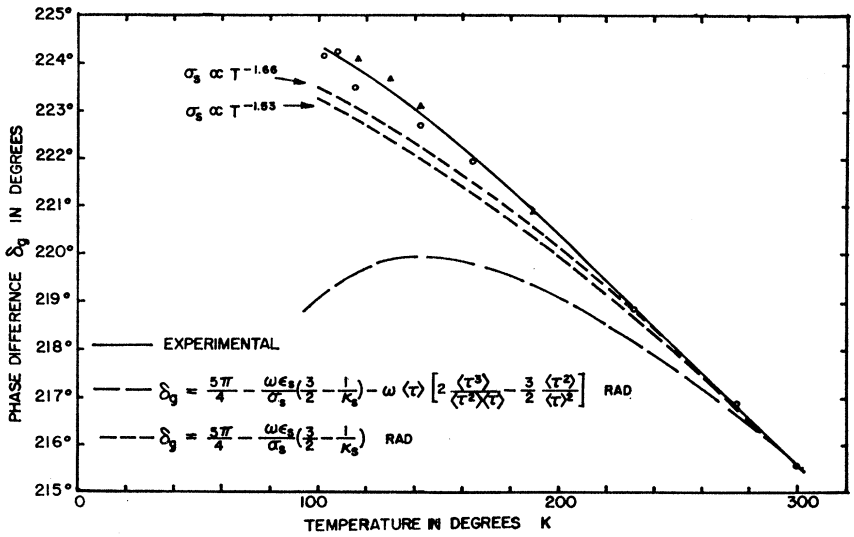

FIG. 10. Graph of δ_g versus temperature for germanium sample 2.

IV. SUMMARY AND CONCLUSION

It appears that, at room temperature, the simple energy-independent scattering model is adequate to describe the magneto-Kerr effect for the range $\sigma_s/\omega\epsilon_s \gg 1$, $\mu_H B \ll 1$, and $\omega\tau \ll 1$, provided mixed scattering is considered in determining the Hall mobility. In this range the approximate expressions for R and δ closely fit the exact expressions from which they were obtained. A mode correction factor can be used to make the plane-wave analysis applicable to the TE_{11} mode in a circular waveguide. If this mode correction factor is considered, theoretical predictions are in good agreement with experimental results at room temperature. The condition of the semiconductor surface, provided it is flat and sufficiently smooth, is not of significant importance in these results. The variation of R with temperature was in accordance with the theory, but poor agreement was found between experimental and theoretical variation of δ with temperature.

APPENDIX A: ELEMENTS OF THE CONDUCTIVITY TENSOR

The real and imaginary parts of the elements of the high-frequency magnetoconductivity tensor, Eq. (1), are listed for the case of energy-dependent τ and the static magnetic field in the [100] crystallographic direction for n-type germanium, the [111] for n-type silicon, or any axis for n-type indium antimonide (where spherical constant-energy surfaces are assumed):

$$\sigma_{11}' = (ne^2/m_\sigma)\langle\tau[1+(\omega\tau)^2+(\omega_c\tau)^2]S^{-1}\rangle, \quad \text{(A1)}$$

$$\sigma_{11}'' = (ne^2/m_\sigma)\omega\langle\tau^2[1+(\omega\tau)^2-(\omega_c\tau)^2]S^{-1}\rangle, \quad \text{(A2)}$$

$$\sigma_{12}' = -(ne^2/m_c)\omega_c\langle\tau^2[1-(\omega\tau)^2+(\omega_c\tau)^2]S^{-1}\rangle, \quad \text{(A3)}$$

$$\sigma_{12}'' = 2(ne^2/m_c)\omega\omega_c\langle\tau^3 S^{-1}\rangle, \quad \text{(A4)}$$

here

$$S = [1+(\omega\tau)^2+(\omega_c\tau)^2]^2 - 4(\omega\tau)^2(\omega_c\tau)^2. \quad \text{(A5)}$$

The m_σ and m_c are the conductivity effective mass and the cyclotron effective mass, respectively, and are given for the case of the n-type germanium or silicon by

$$m_\sigma = 3m_T m_L/(m_T+2m_L), \quad \text{(A6)}$$

$$m_c = [3m_T^2 m_L/(2m_T+m_L)]^{1/2}, \quad \text{(A7)}$$

where the particular magnetic field orientations specified have been assumed for Eq. (A7). For the case of spherical constant-energy surfaces, $m_\sigma = m_c = m^*$.

APPENDIX B: THE EXPRESSIONS FOR ROTATION AND ELLIPTICITY IN TERMS OF R AND δ

The ellipticity ϵ of the reflection ellipse is defined as the ratio of the minor to the major axis. The angle of rotation θ is the angle that the major axis of the reflection ellipse makes with the incident plane of polarization. For the case where R is small, θ and ϵ are related to R and δ by the following approximate expressions:

$$\theta \approx R\cos\delta, \quad \text{(B1)}$$

$$\epsilon \approx R\sin\delta. \quad \text{(B2)}$$

These relations apply to the case of guided waves as well as to plane waves. If R is not small the exact relations must be used.[11]

APPENDIX C: CONSIDERATION OF MULTIPLE REFLECTIONS

If the semiconductor sample is less than about 5 skin-depths thick, the effect of multiple reflections within the crystal must be taken into account in determining the magneto-Kerr effect. To include the effects of multiple reflections, the $\rho_\pm$ in Eqs. (4) and (5) must be replaced by

$$r_{c_\pm} = (\rho_\pm - e^{-i2k_\pm d})/(1-\rho_\pm e^{-i2k_\pm d}) \quad \text{(C1)}$$

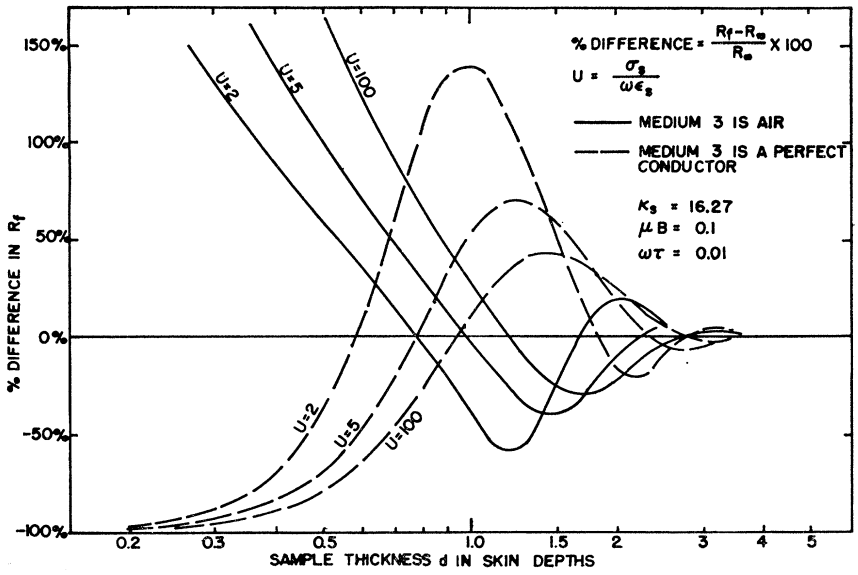

FIG. 11. Graph of % difference in R_f from R_∞ versus sample thickness for germanium.

for the case where the medium behind the semiconductor is a perfect conductor. If the medium behind the sample is air followed by a perfectly absorbing medium, the $\rho_\pm$ in Eqs. (4) and (5) should be replaced by

$$r_{0_\pm}=\rho_\pm[(1-e^{-i2k_\pm d})/(1-\rho_\pm^2 e^{-i2k_\pm d})]. \quad \text{(C2)}$$

Let R_f represent the value of R for a sample of finite thickness in which multiple reflections are to be considered. For emphasis, let R_∞ be the value of R for a sample which is, for practical purposes, infinitely thick. The percent difference in R_f relative to R_∞ is plotted in Fig. 11 as a function of the thickness of the finite sample in skin depths. Note that for sample thickness greater than about 5 skin depths there is no significant difference from the infinitely thick sample. For a guided wave, $k_\pm$ should be replaced by $k_{g\pm}$ in Eqs. (C1) and (C2), and used along with k_{g0} in calculating $\rho_\pm$.

ACKNOWLEDGMENTS

The authors are indebted to Dr. J. K. Furdyna for many valuable discussions. We are also grateful to W. B. Haynes of Mallinchrodt Chemical Works for several of the silicon crystals and to D. E. Thomas, Jr., of Sylvania Electrical Products, Inc. for several germanium crystals.